Deterministic and stochastic models of intracellular Ca^{2+} waves

2003 New J. Phys. 5 96

(http://iopscience.iop.org/1367-2630/5/1/396)

New Journal of Physics
An Institute of Physics and Deutsche Physikalische Gesellschaft Journal

Deterministic and stochastic models of intracellular Ca^{2+} waves

M Falcke
Hahn Meitner Institute, Glienicker Straße 100, 14109 Berlin, Germany
E-mail: falcke@hmi.de

New Journal of Physics **5** (2003) 96.1–96.28 (http://www.njp.org/)
Received 10 January 2003
Published 22 July 2003

Abstract. Intracellular Ca^{2+} dynamics allows for the observation of wave formation from elemental release events to the global phenomenon. It shows propagating waves with deterministic features and at the same time probabilistic behaviour like variable periods. Formulation and analysis of deterministic wave models sheds new light on experimental observations and contributes to the theory of nonlinear propagating waves by exhibiting new instabilities. That is demonstrated with the example of Ca^{2+} waves with energized mitochondria. Stochastic models can describe spatio-temporal structures from localized puffs to propagating waves. They explain the origin of long timescales in Xenopus oocytes and wave generation. The implications of the results of both approaches for the theory of intracellular Ca^{2+} dynamics is discussed.

Contents

PII: S1367-2630(03)58127-7

Calcium is a ubiquitous second messenger which regulates multiple cellular functions. It is involved in processes as different as muscle contraction and synaptic transmission [1, 51]. Ca^{2+} has a crucial role at the beginning of life in the activation of eggs after fusion of the sperm [71] and controls cell differentiation later on in development [37]. It was called the 'life and death signal' by Berridge *et al* [6] because of this paramount importance in the regulation of cells.

The Ca^{2+} signal employed by such a variety of cells and processes is a transient increase of the intracellular concentration. This Ca^{2+} increase is due to influx through the cell membrane or to Ca^{2+} release from internal stores. The release from internal stores like the endoplasmic reticulum (ER) or the sarcoplasmic reticulum into the cytosol is a nonlinear process. It leads in many cells to the formation of spatio-temporal signals in the form of waves of high Ca^{2+} concentration travelling across the cell. Intracellular calcium waves were first observed in medaka eggs [76] and later on in Xenopus oocytes (frog eggs) [33, 57], hepatocytes [70], articular chondrocytes [18] and cardiac myocytes [72, 101].

The opening and closing of Ca^{2+} channels controls the release. These channels are closely packed into clusters on the ER membrane [63, 64, 92, 96]. The maximal number of channels in a cluster is not known but is estimated to be in the range of 20–30 [10, 26, 92]. The clusters are randomly distributed. Areas with high cluster density are called focal sites [11, 57, 66]. The average distance of clusters outside focal sites in Xenopus oocytes has been determined as 7.3 μm and inside focal sites as 5 μm [66]. Channels open and close stochastically. Stochastic behaviour manifests itself as spontaneous release events through single channels or several channels in a cluster [7, 11, 66, 92, 97].

A channel type present in the ER membrane of many cells is the inositol 1,4,5-trisphosphate (IP_3) receptor channel (IP_3R). The open probability of the IP_3R depends on the calcium concentration on the cytosolic side of the channel and the IP_3 concentration (see [74, 95] for a review). It increases nonlinearly with the IP_3 concentration and the Ca^{2+} concentration. Hence, Ca^{2+} released by one channel increases the open probability for neighbouring channels. That provides a self-amplifying release mechanism. Very high Ca^{2+} concentration inhibits the channel and terminates release.

It has been suggested that the Ca^{2+} content of the ER may regulate the IP_3R open probability [14, 69]. However, that could only be observed if the store was less than 30% full [73]. The Ca^{2+} binding site on the lumenal face of the IP_3R has too low an affinity to serve as a sensor [87]. Many effects attributed to lumenal Ca^{2+} can be explained as being exerted by released Ca^{2+} on the cytosolic side as well [95] and several studies come to the conclusion that regulation by lumenal ER Ca^{2+} is not an essential component of the release control [43, 44, 95]. Hence, especially since we will not consider release emptying stores to less than 30% of their content, we assume that lumenal Ca^{2+} does not control IP_3 receptor channel open probability.

Another element of intracellular Ca^{2+} handling are buffers. Buffers are proteins binding most of the Ca^{2+} in a cell (up to 99%). They are present in the cytosol as well as the ER. Buffers are considered as mobile or immobile depending on their diffusion characteristics. The rate constants of Ca^{2+} binding and dissociation allow for a distinction between slow and fast buffers.

The dependence of the open probability of the release channels on cytosolic Ca^{2+} creates communication between channels and allows for the formation of spatio-temporal patterns of intracellular Ca^{2+} release. These patterns show a hierarchy of phenomena. The smallest event is the opening of a single channel, called a blip. The next larger event is a puff and is the opening of several closely packed channels. Puffs can cooperate to set off a wave travelling through the cell. Waves would appear as an elevation of the Ca^{2+} concentration engulfing the whole volume in

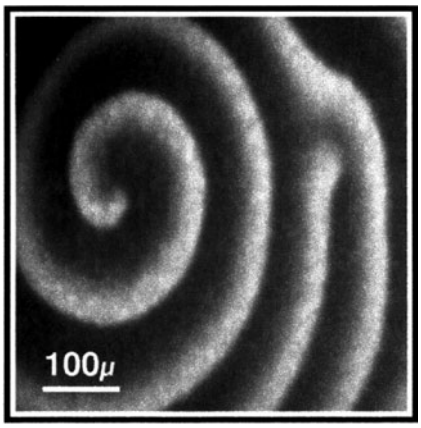

Figure 1. Spiral wave in a Xenopus oocyte. Bright areas indicate high Ca^{2+}. The wave was observed under conditions of increased SERCA density (figure from [30]). See animation.

cells smaller than the wavelength. If waves occur periodically, they appear as global oscillations. The type of the dominant pattern depends on the IP_3 concentration with puffs at low and waves and oscillations at high values.

Mitochondria are involved in energy-yielding metabolism. They contain many enzymes that together catalyze the oxidation of organic nutrients by molecular oxygen. The energy gain from oxidation is used for ATP synthesis. The transport of different chemical species involved in that process across the mitochondrial membrane and the dynamics of the membrane voltage was described in comprehensive models by Magnus *et al* and Selivanov *et al* [59, 60, 61, 84]. In the course of these processes, mitochondria take up and release Ca^{2+} and thus modulate intracellular Ca^{2+} signals [9, 20, 22, 30, 34, 40, 41, 45, 48, 68, 77]. Especially (but not only) Friel pointed out that modulation occurs in two ways: a buffer-like action due to Ca^{2+} uptake and a slowing of the decay of cytosolic transients due to mitochondrial release [15, 16, 34].

Most of the theoretical research has focused on deterministic models of intracellular Ca^{2+} waves [3, 23]–[25, 29, 89, 90, 99, 100]. Only recently, the stochastic nature of intracellular Ca^{2+} release has been considered [27, 28, 32, 52, 85]. This development of research reflects the character of Ca^{2+} dynamics with its stochastic and deterministic features. The elemental release events can be observed as puffs occurring spontaneously and with an exponential distribution for the interval between puffs. At slightly different parameters, these puffs build up waves with constant velocity and smooth wavefront and -back (see figure 1). The single puffs can still be observed if the observation zooms in and a wave travels through the area of interest [66]. This possibility to observe the elemental events building global phenomena is one of the most fascinating features of intracellular Ca^{2+} dynamics.

We discuss an example from deterministic modelling dealing with waves under conditions of energized mitochondria. That example was chosen so as to illustrate basic features of the modelling and because it explains surprising experimental results while revealing a phenomenon new to the theory of pattern formation as well: a gap in the dispersion relation. Then, we look at stochastic modelling, how long timescales can arise from stochasticity and the impact of channel numbers on wave characteristics. In the concluding section we discuss the relation between the models and current problems.

1. Mitochondria shape waves

Jouaville *et al* [48] carried out experiments investigating the role of mitochondria in pattern formation in Xenopus oocytes. Energization of mitochondria by injection of pyruvate/malate abolished spiral patterns but not waves in general. The waves forming the pattern under these conditions showed longer periods, higher amplitudes and higher velocities. Spiral waves could be restored when pump density was increased by overexpression of SERCAs [30, 48].

Energization of mitochondria results in an increase of the mitochondrial effective membrane potential from -92 to about -120 mV. The mitochondrial matrix is negative relative to the surrounding cytosol. That leads to increased Ca^{2+} uptake through the uniporter. Intuitively, we would expect a decrease of amplitudes and wave velocities upon energization of mitochondria. Indeed, that is what was observed in rat cortical astrocytes [22]. The wave velocity and amplitude increased upon collapsing the mitochondrial membrane potential and thus abolishing mitochondrial Ca^{2+} uptake. This action of mitochondria corresponds to their behaviour analogous to buffers. However, we will see that in the experiments in Xenopus oocytes the other characteristic modulation of cytosolic Ca^{2+} transients by mitochondria—the biphasic decay [16]—comes into play.

The model by Falcke *et al* [30] focuses on Ca^{2+} uptake and release of mitochondria only to obtain a simple model explaining the impact of increased mitochondrial activity on Ca^{2+} wave patterns in Xenopus oocytes. The model neglects the mitochondrial membrane potential dynamics. That can be justified by the results of Magnus and Keizer [59]–[61] who simulated membrane potential dynamics with a more detailed model and found that it changes by about 2% only under normal conditions. Furthermore, Friel *et al* [16] were able to fit experimental results of mitochondrial fluxes with excellent agreement to expressions for the currents neglecting membrane potential as well.

We extend the Othmer–Tang model [94] to incorporate the mechanisms of mitochondrial Ca^{2+} cycling by adding a third equation governing the uptake and release of mitochondrial Ca^{2+} (denoted m) and a corresponding term in the differential equation for cytosolic Ca^{2+} (c) [30]. The first term of the m-dynamics is Ca^{2+} uptake through the uniporter, the second one release through the Na^+/Ca^{2+} exchanger [30]. These terms appear again in the cytosolic dynamics. The variable c denotes the cytosolic Ca^{2+} concentration. The cytosolic dynamics includes diffusion, a leak flux, the c-dependent channel flux and removal of Ca^{2+} from the cytosol by pumps. The first rhs term in equation (1) models Ca^{2+} diffusion in the cytosol. The second term describes Ca^{2+} release from the ER by leak flux (P^{leak}) and channel flux (P^{chan}) controlled by the fraction of inhibited channels $(1-n)$ and the fraction of channels with activating Ca^{2+} and IP_3 bound $(c/(c+\beta_1(1+\beta_0(I)))$. The Othmer–Tang model assumes that the receptor channel has a binding site for IP_3, an activating binding site for Ca^{2+} and an inhibiting binding site for Ca^{2+}. The channel opens upon binding of IP_3 and Ca^{2+} to the activating site. Inhibition is provided by a second Ca^{2+} binding site. If Ca^{2+} is bound to the inhibiting site, the channel is closed. Binding to the inhibiting site occurs on a slower timescale and with lower affinity. Hence, an adiabatic elimination of the activating Ca^{2+} and IP_3 binding processes can be applied leading to the dependence of the channel flux on Ca^{2+} and IP_3 given above. The third term (P^{max}) models the uptake of Ca^{2+} into the ER by ATPases (see [58]). The fourth and fifth terms are the contribution of mitochondria. The dynamics of the fraction of inhibited channels n is a relaxation to its Ca^{2+}-dependent asymptotic value:

$$\begin{aligned}
\frac{\partial c}{\partial t} &= D\Delta c + \left(P^{\text{leak}} + P^{\text{chan}}\frac{c(1-n)}{c+\beta_1(1+\beta_0(I))}\right)((1+\nu_{\text{m}}+\nu_r)C_{\text{M}} - \nu_{\text{m}}m - (1+\nu_r)c) \\
&\quad - \nu_r P^{\max}\frac{c^2}{(K^M)^2+c^2} - \nu_{\text{m}}\left(V_{\max}^{(1)}\frac{c^2}{K_{\text{d}}^2+c^2} - V_{\max}^{(2)}\frac{\text{Na}^2}{K_{\text{Na}}^2+\text{Na}^2}\frac{m}{K_{\text{m}}+m}\right) \\
\frac{\partial n}{\partial t} &= \varepsilon\left(\frac{(1-n)c^2}{\beta_2[c+\beta_1(1+\beta_0(I))]} - n\right) \\
\frac{\partial m}{\partial t} &= V_{\max}^{(1)}\frac{c^2}{K_{\text{d}}^2+c^2} - V_{\max}^{(2)}\frac{\text{Na}^2}{K_{\text{Na}}^2+\text{Na}^2}\frac{m}{K_{\text{m}}+m}.
\end{aligned} \tag{1}$$

Parameters are explained in table 1. The equation for mitochondrial dynamics essentially follows the data presented in the experimental review by Gunter and Pfeiffer [39]. Measured values of the half-maximum value K_{d} for the uniporter from 1 to 189 μM are reported in this review. Values at the upper end of this range would not allow the uniporter to transport Ca^{2+} during physiological Ca^{2+} transients. Physiological evidence in many cell types shows that mitochondria respond to physiological Ca^{2+} transients [2, 4, 5, 15, 17, 34, 36, 38, 42, 48, 75, 78, 80, 82, 88, 93]. That suggests K_{d} values in the range of concentrations occurring during cytosolic Ca^{2+} transients to apply in this situation as explicitly stated in [75]. Alternatively, mitochondria might experience Ca^{2+} concentrations much larger than the average bulk concentration. There is morphological evidence [21, 36, 41, 79, 83, 88] showing mitochondria in close proximity to the ER, where they experience Ca^{2+} concentrations considerably higher than those in bulk cytoplasm. Rizzuto *et al* [78, 80] estimated that the uptake of Ca^{2+} released from internal stores was an order of magnitude faster than that resulting from the average bulk concentration of Ca^{2+}. Such a difference to bulk concentration can be included into a model by assuming the concentration at the mitochondrial uniporter always to be by a fixed factor larger than the bulk concentration. That results in re-scaling of K_{d} by this factor. Either way leads to a small half-maximum value of K_{d} for mitochondrial Ca^{2+} uptake in the model. Similar conclusions were drawn by Sneyd *et al* [91]. Mitochondria in Xenopus oocytes have an average distance from release sites of 2.3 μm, which is not very close in terms of the diffusion length of free Ca^{2+} in the cytosol and the argument of close proximity does not apply [67]. On the other hand, puff sites spaced less than 2.2 μm apart showed high correlation in their activity [102]. That means mitochondria are within the length scale of Ca^{2+} increases at least sufficient to set off a puff. The other parameter of the uniporter dynamics, $V_{\max}^{(1)}$, is varied to model the increase in membrane potential due to injection of pyruvate/malate.

The buffer-like action of mitochondria can best be observed for solitary waves since their velocity is not influenced by the dispersion relation, unlike waves in a periodic wave train. Increasing mitochondrial uptake slows down propagation of solitary waves and decreases wave amplitude (figure 2). That is analogous to the effect of buffers on wave speed [46, 89, 99]. Waves in astrocytes showed an increase of wave velocity and amplitude when the mitochondrial potential was collapsed (using antimycin A1 with oligomycin) corresponding to a decrease of $V_{\max}^{(1)}$ from some positive value to 0 in our terms [22]. This observation is compatible with the results shown in figure 2. Similarly, the observation of mitochondria limiting spatial spread of release activity found in pancreatic acinar cells would be in agreement with the buffer mode [98]. However, reduction of velocity and amplitude is not the major effect observed in Xenopus oocytes.

In Xenopus oocytes, stable spirals are observed under conditions of low mitochondrial Ca^{2+} uptake [13, 48, 54, 55]. Spiral waves are periodic patterns, unlike the solitary waves mentioned above. In simulations of this regime, a decrease in rotational frequency of spiral waves is

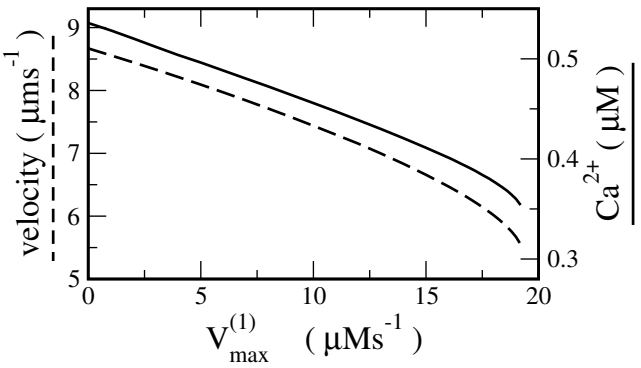

Figure 2. Characteristics of solitary waves in dependence on $V_{\max}^{(1)}$. Waves slow down with increasing mitochondrial uptake and finally fail to propagate. Parameter values are given in table 1 except $P_r^{\max} = 7.03\ \mu\mathrm{M\ s^{-1}}$, $C_\mathrm{M} = 1.2\ \mu\mathrm{M}$, $I = 0.27\ \mu\mathrm{M}$ and $\nu_\mathrm{m} = 0.15$.

Table 1. Parameters for deterministic simulations.

Parameter	Value	Unit
Leak flux coefficient P_r^{leak}	0.0097	$\mathrm{s^{-1}}$
Channel flux coefficient P_r^{chan}	3.89	$\mathrm{s^{-1}}$
Pump flux coefficient $P_r^{\max}$	5.31	$\mu\mathrm{M\ s^{-1}}$
Pump dissociation constant K_r	0.0296	$\mu\mathrm{M}$
Uniporter flux coefficient $V_{\max}^{(1)}$	6	$\mu\mathrm{M\ s^{-1}}$
Uniporter dissociation constant K_d	1.5	$\mu\mathrm{M}$
Na^+/Ca^{2+} exchanger flux coefficient $V_{\max}^{(2)}$	3	$\mu\mathrm{M\ s^{-1}}$
Na^+/Ca^{2+} exchanger Ca^{2+} dissociation constant K_m	1	$\mu\mathrm{M}$
Na^+/Ca^{2+} exchanger Na^+ dissociation constant K_Na	5	mM
Na^+ concentration	10	mM
Effective diffusion coefficient D of Ca^{2+}	50	$\mu\mathrm{m^2\ s^{-1}}$
Effective volume ratio $\nu_r = V_\mathrm{ER}/V_\mathrm{cyt}$	0.185	
Effective volume ratio $\nu_\mathrm{m} = V_\mathrm{mit}/V_\mathrm{cyt}$	0.1	
Total concentration of Ca^{2+} C_M	1.56	$\mu\mathrm{M}$
IP_3 concentration I	0.27	$\mu\mathrm{M}$
Subunit kinetics		
β_0	$0.8\ \mu\mathrm{M}/I$	
β_1	0.12	$\mu\mathrm{M}$
β_2	0.1	$\mu\mathrm{M}$
ε	0.15	$\mathrm{s^{-1}}$

accompanied by a small increase in wave velocity and a small decrease in wave amplitude with increasing $V_{\max}^{(1)}$ (figure 3). However, this behaviour only holds for small values of $V_{\max}^{(1)}$ below a critical value. When mitochondria are energized in Xenopus oocyte experiments, spiral wave patterns become unstable, disappear, and do not reform. In agreement with experiments, spirals cease to exist at a certain critical value of mitochondrial Ca^{2+} uptake $V_{\max,\mathrm{cr}}^{(1)}$ in simulations too. Above this value, it is found that waves emitted from pacemakers form the pattern. Examples of these waves, as observed in experiments and simulations, are shown in figure 4.

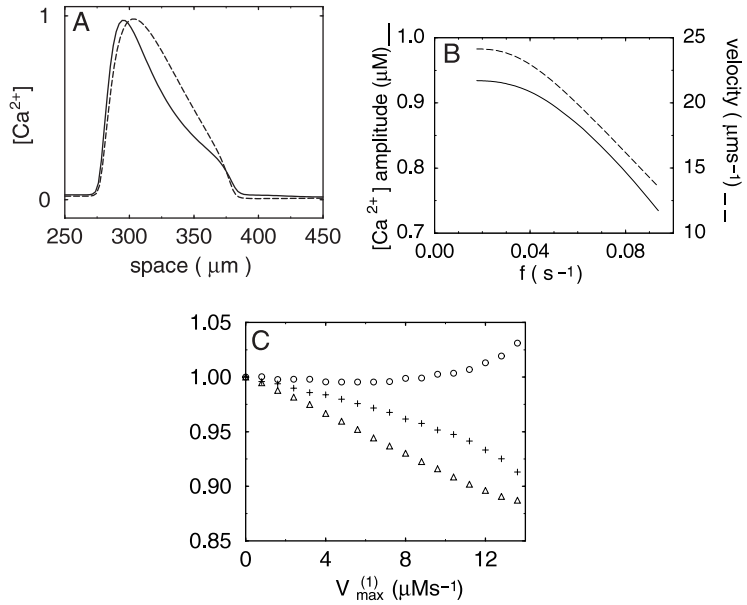

Figure 3. Characteristics of waves with increased mitochondrial activity: (A) pulse profiles with (full curve, $V^{(1)}_{\max} = 28\ \mu\mathrm{M\ s^{-1}}$) and without (dashed curve, $V^{(1)}_{\max} = 0\ \mu\mathrm{M\ s^{-1}}$) increased mitochondrial activity. The amplitudes were normalized to 1. The direction of motion is from right to left. With increased mitochondrial activity the typical biphasic decrease of Ca^{2+} in the back of the pulse can be seen. In the refractory area (around 400 μm), Ca^{2+} is higher with increased mitochondrial activity than under normal conditions. That prolongs receptor recovery. (B) Pulse amplitude (full curve) and velocity (dashed curve) for periodic pulse trains in dependence on the frequency of the wave train, $V^{(1)}_{\max} = 8\ \mu\mathrm{M\ s^{-1}}$. (C) Dependence of spiral wave velocity (circles), frequency (crosses) and amplitude (triangles) on $V^{(1)}_{\max}$ for low mitochondrial Ca^{2+} uptake ($V^{(1)}_{\max} < V^{(1)}_{\max,\mathrm{cr}}$) normalized to the value at $V^{(1)}_{\max} = 0$. For parameters see table 1. (Figure from [30].)

A simulation was also carried out corresponding to an experiment in which pyruvate/malate was injected into an oocyte [48]. In the course of this simulation, $V^{(1)}_{\max}$ was increased to mimic the injection. The changing Ca^{2+} concentration at a location about a wavelength off the spiral core is shown in figure 4(C). The Ca^{2+} oscillations associated with spiral waves cease as the system moves to a new steady state upon increasing $V^{(1)}_{\max}$. This is followed by the dominance of waves emitted from a pacemaker. Figure 5 shows the transient state of a spiral wave tip when Ca^{2+} uptake exceeds the critical value ($V^{(1)}_{\max} > V^{(1)}_{\max,\mathrm{cr}}$).

When the tip bends in the early stage of spiral formation, another small-amplitude wave emerges from the back of the wave at the highest curvature (indicated by white arrow in figure 5(A)). Mitochondrial Ca^{2+} efflux is responsible for this secondary wave, which in turn is responsible for prolonging the refractory state of the IP_3R and preventing spiral formation. Although efflux plays a fundamental role in the destabilization of the spiral core, it is not the sole determinant. Here, wavefront curvature also contributes to spiral core instability. Near the spiral tip, where the wavefront curvature is the highest, Ca^{2+} diffusion down the gradient of the

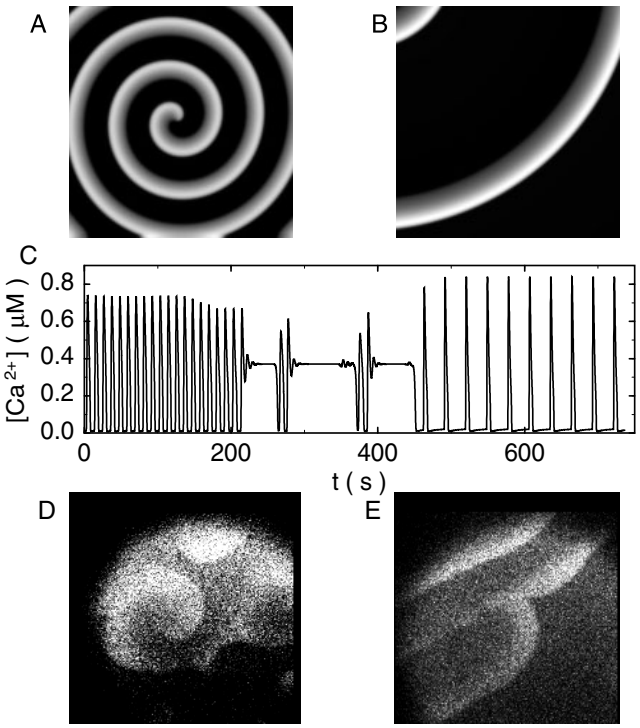

Figure 4. Simulation of an experiment. (A), (B) and (C) are results of a simulation. (D) and (E) are pictures from experiments. (A), (D) Spiral at low mitochondrial activity. There is a pacemaker in the upper left corner of (A) but its activity is suppressed by the spiral ($V_{\max}^{(1)} = 8\ \mu\mathrm{M\ s^{-1}}$). (C) Time course of the local Ca^{2+} at a point two spiral wavelengths off the centre of the simulation area. $V_{\max}^{(1)}$ was increased at $t = 120$ s to 16 $\mu\mathrm{M\ s^{-1}}$. That corresponds to the injection of pyruvate/malate in the experiments. The spiral becomes unstable and disappears. After a transient, the pacemaker governs the pattern formation. See animation. (B), (E) Waves emitted from a pacemaker in the regime with high mitochondrial activity. The other parameter values are the same as in figure 3. For other parameters see table 1. (Figure from [30].)

back of the wave is focused. This focal increase in Ca^{2+} further prolongs the refractory period of IP_3Rs. Thus, both curvature and mitochondrial efflux are responsible for the generation of the secondary wave which forces the tip outward, thereby preventing spiral pattern formation (figure 5(B)). This phenomenon was experimentally observed in the oocyte after energization as shown in figures 5(C) and (D). The free end of a Ca^{2+} wave is forced outward by a secondary Ca^{2+} wave and the spiral fails to form.

When periodic wave patterns of different frequencies are present in a medium, they compete for space. As time goes on, the pattern with the highest frequency generally gains spatial control of the field. It was shown experimentally that pacemakers are present in oocytes and that spiral waves dominate pacemakers in Xenopus oocytes with normal mitochondrial respiration [56]. Thus, it is only after the spirals have disappeared above $V_{\max,\mathrm{cr}}^{(1)}$—when mitochondria are energized—that the lower frequency pacemakers can govern the pattern formation in the oocyte. Hence, energization results in a wave pattern dominated by slow pacemakers. The smaller

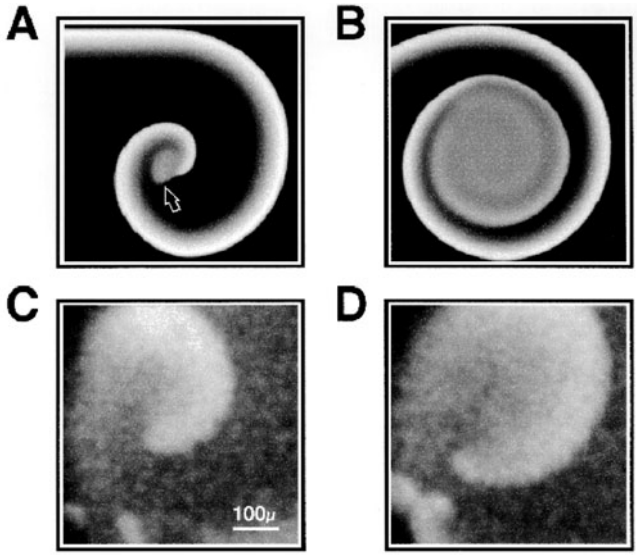

Figure 5. Development of the core of an unstable spiral at high mitochondrial activity ($V_{\max}^{(1)} = 8\ \mu\mathrm{M\ s^{-1}}$; the other parameter values are the same as in figure 3). (A) and (B) are taken from simulations, (C) and (D) from experiment. (A), (C) When the wave bends at its free end, a patch of high Ca^{2+} emerges at its back. (B), (D) The patch expands, pushing the free end outward and preventing spiral formation. For other parameters see table 1. (Figure from [30].)

frequency leads to an increase in wave amplitude and velocity, according to the dispersion relation (figure 3).

The local dynamics of the model yield three stationary states, each with different concentrations of cytosolic Ca^{2+}. At low mitochondrial Ca^{2+} uptake (small $V_{\max}^{(1)}$), only the state with the lowest cytosolic Ca^{2+} is stable and the cytosol behaves as an excitable system (figure 6). The system becomes bistable at the uptake value $V_{\max,b}^{(1)}$ (note, $V_{\max,b}^{(1)} < V_{\max,cr}^{(1)}$). At this point, the stationary state with the highest cytosolic Ca^{2+} concentration is stabilized by increased mitochondrial Ca^{2+} cycling.

When both stable stationary states exist at adjacent locations, the front connecting the states moves so that the volume occupied by one of the states grows at the expense of the other. The state which loses volume is metastable. Whether the system switches by a front from low to high cytosolic Ca^{2+} or vice versa depends on the degree of mitochondrial energization. In most of the bistable region that we consider here, the state of high cytosolic Ca^{2+} is metastable. Note that in the bistable regime, both pulses and fronts occur and below $V_{\max,cr}^{(1)}$ spirals form. Above $V_{\max,cr}^{(1)}$, the region of high Ca^{2+} can expand if it is surrounded by a pulse, even though it is the metastable state. Thus, a front of transition from low to high Ca^{2+} can occur in this parameter range if the front immediately follows a pulse. This occurs when the unstable spiral core expands (figures 5(A)–(D)). If the pulse leading the front is extinguished by collision with another pulse, the front reverses its direction of motion and the patch of high Ca^{2+} shrinks and disappears. Another way that a patch of high Ca^{2+} in figure 5(B) may disappear is that a pacemaker inside it starts a front that returns the cytosol to a state of low Ca^{2+}. Finally, energization of mitochondria creates a pattern in which not spirals but the waves emitted by pacemakers become the dominant structure of the bistable system.

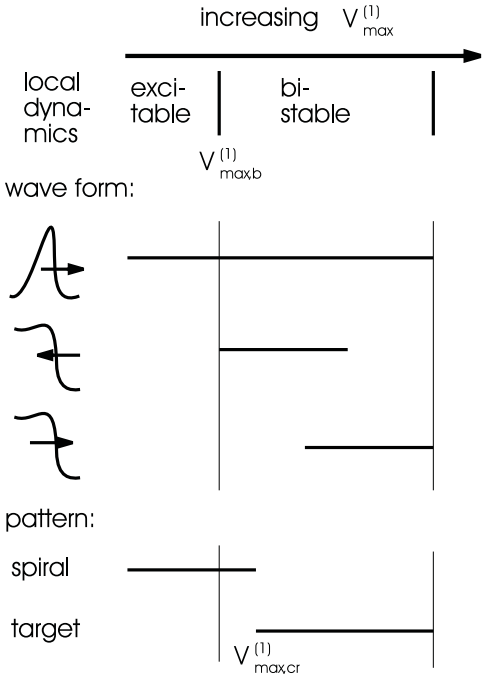

Figure 6. Survey of the behaviour of the local dynamics, wave form existence and patterns of the equation (1) with increasing $V^{(1)}_{max}$.

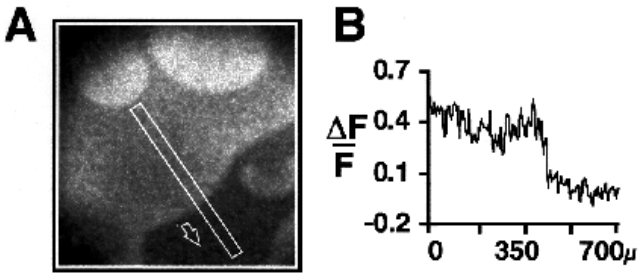

Figure 7. Experimentally observed Ca^{2+} front travelling into the region with low Ca^{2+}. (A) Bright areas indicate high Ca^{2+}. (B) Line scan along the bar indicated in (A). (Figure from [30].)

At very high energization of the mitochondria, fronts from low to high cytosolic Ca^{2+} continue to exist outside the spiral core. The region of high cytosolic Ca^{2+} emerging from the spiral instability continues to expand even if the leading pulse becomes annihilated. Experimental evidence for such a transition in oocytes is shown in figure 7. Fronts in both directions (and pulses) co-exist before at still even higher $V^{(1)}_{max}$ fronts switching the cytosol from high to low Ca^{2+} cease to exist. If a front is initiated in this range of $V^{(1)}_{max}$, the resting Ca^{2+} concentration in the oocyte is predicted to switch to the stationary state with high cytosolic Ca^{2+} and wave activity stops. That is evocative of the fertilization wave in oocytes which was modelled as a bistable system too [33, 100].

The mechanism of mitochondrial-induced spiral instability described above suggests that spirals could be recovered by increasing cytosolic Ca^{2+} removal. Experimental studies in

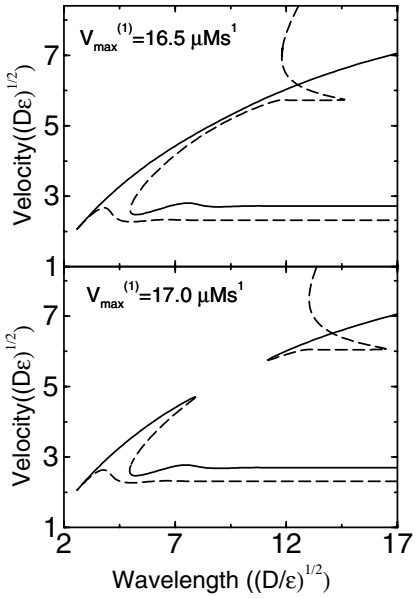

Figure 8. Branches of wave train solutions of equation (1) for $V_{\max}^{(1)} = 16.5$ and 17.0 μM s^{-1}. Dashed curves indicate unstable solutions, full curves stable ones. For the other parameters see table 1. (Figure from [31].)

Xenopus oocytes show that overexpression of SERCAs permits spiral wave formation even in the presence of energized mitochondria. Consistent with experimental observations, simulations showed that an increase in SERCA density restores spiral formation at high mitochondrial Ca^{2+} uptake [30].

In summary, the model consisting of equations (1) could cast the main experimental findings into a unified picture. It is worth asking whether mechanisms can be identified underlying the wave instabilities observed in simulations [31]. For the presentation of these results we change to dimensionless variables and measure space units in $\sqrt{D/\epsilon}$ and time units in $1/\epsilon$. The Ca^{2+} concentration is given in units of C_{M}.

We investigate the existence and stability of a pulse with periodic boundary conditions for a range of $V_{\max}^{(1)}$ in the bistable regime (see figure 8). Waves are found as stationary solutions in the co-moving coordinate system. There are four branches of periodic solutions with stable and unstable parts originating from two saddle-node bifurcations at small wavelengths (see figure 8) [31]. The 'inner' pair of branches—formed by the unstable high-velocity branch and the stable low-velocity branch (see figure 8, top)—does not exist at low $V_{\max}^{(1)}$. The high-velocity branches correspond to a range of high Ca^{2+} travelling in a medium in the lower stationary state (see figure 9, right). The wave trains forming the outer part of spirals are on the stable branch. The unstable high-velocity pulses are distinguished from the stable ones by a delayed drop of the Ca^{2+} concentration to the level of the refractory area and a correspondingly shorter refractory area. The low-velocity branch is a range of low Ca^{2+} travelling in a medium in the upper stationary state (see figure 9, left).

At a certain value of $V_{\max}^{(1)} = V_{\max,\mathrm{tc}}^{(1)} = 16.9\ \mu$M s^{-1}, the stable high-velocity branch collides with the unstable one and a gap in velocity opens up (figure 8, bottom). The collision of the branches is a transcritical bifurcation at parameters $(V_{\max,\mathrm{tc}}^{(1)}, \lambda_{\mathrm{tc}})$, where the wavelength λ of the

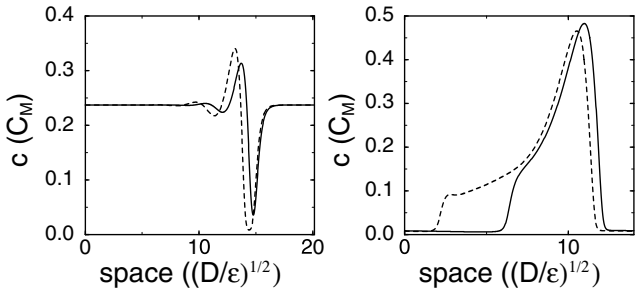

Figure 9. Profiles of coexisting wave trains travelling from left to right at $V_{\max}^{(1)} = 17.0\ \mu\mathrm{M\ s^{-1}}$. Full curve: stable; dashed curve: unstable; left panel: low-velocity branches; right panel: high-velocity branches. For other parameters see table 1. (Figure from [31].)

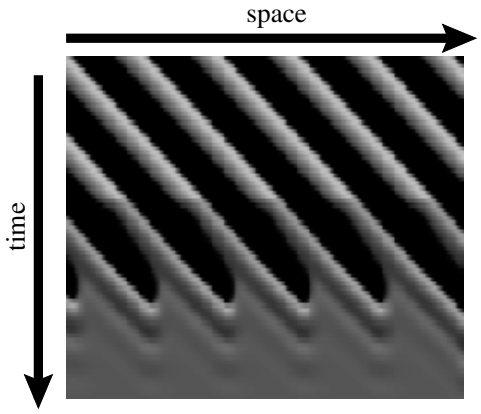

Figure 10. A periodic wave train on a ring disappears upon a parameter shift from $V_{\max}^{(1)} = 16.5$ to $17.0\ \mu\mathrm{M\ s^{-1}}$, because of the opening dispersion gap. Bright areas indicate high Ca^{2+}. The peak grey level changes at the moment of the parameter shift. For the other parameters see table 1. (Figure from [31].)

wave trains has to be considered as an additional bifurcation parameter. The situations above and below $V_{\max,\mathrm{tc}}^{(1)}$ shown in figure 8 represent the typical unfoldings of this bifurcation with respect to the branches involved in the collision. The dispersion gap creates a range of forbidden periods. In figure 10 we show a simulation of a wave train where $V_{\max}^{(1)}$ is shifted from 16.5 to $17.0\ \mu\mathrm{M\ s^{-1}}$ with a period in the opening gap. Shortly after the parameter shift, the wave train disappears by flooding the refractory area with Ca^{2+}. This is caused by strong Ca^{2+} release from the mitochondria and is in agreement with the spiral instabilities described above.

The mechanism destroying the pulse becomes more plausible by considering the pulse profile and the unstable eigenmode (figure 11). Mitochondria take up a great amount of Ca^{2+} during the first part of the excited phase of the pulse. That mitochondrial Ca^{2+} is released when cytosolic Ca^{2+} decreases in the back of the pulse as can be seen in figure 11, bottom. That slows down the decrease of cytosolic Ca^{2+} in the back. With increasing mitochondrial uptake (i.e. increasing $V_{\max}^{(1)}$) the amount of Ca^{2+} taken up in the first part of the pulse increases and so does the amount released in the back. Finally, at the critical value of $V_{\max}^{(1)}$, the large amount of

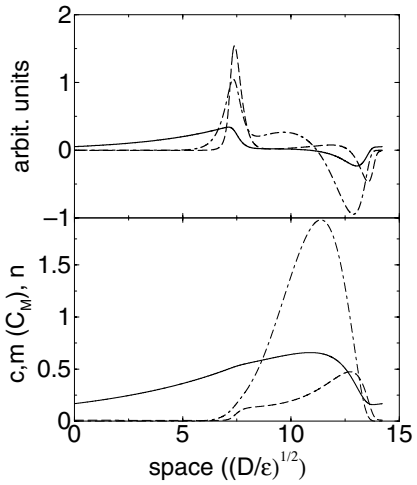

Figure 11. Pulse profile (bottom panel) and eigenmodes (top panel) of an unstable pulse close to the saddle node bifurcation limiting the dispersion gap at high velocities. The pulse travels from left to right. Curve styles: dashed— c, dash-dotted—m, full—n. The most unstable eigenmode is almost identical with the Goldstone mode in the front range but deviates considerably in the back of the pulse. For the other parameters see table 1. (Figure from [31].)

released mitochondrial Ca^{2+} causes a transition to the upper stationary state in the back of the pulse instead of the transition to the refractory state. This mechanism is supported by the shape of the eigenvector of the leading eigenvalue (figure 11, top). A comparison of that eigenmode with the Goldstone mode (not shown), which would cause a simple shift of the pulse, led to the identification of the mechanism in biological terms as prolongation of recovery from inhibition. The eigenmode is identical to the Goldstone mode in the front range of the pulse. However, the unstable mode raises the level of cytosolic Ca^{2+} c where the transition from the excited phase of the pulse to the refractory area occurs and hence increases the inhibitor n in the refractory area of the pulse.

Free spirals at low $V^{(1)}_{\max}$ are stable. With slowly increasing $V^{(1)}_{\max}$, spirals are destroyed at $V^{(1)}_{\max,\mathrm{cr}} < V^{(1)}_{\max,\mathrm{tc}}$. The occurrence of the instability in the spiral core at lower $V^{(1)}_{\max}$ is in agreement with the ideas about the mechanism and due to curvature effects close to the spiral core as explained above. If we stabilize the spiral core artificially, spirals are destroyed when the rim of the dispersion gap reaches their intrinsic period [31].

The dispersion gap can be perceived as a nonlinear frequency filter. Given the fact that waves on the lower branch of the dispersion relation cannot exist in two or more spatial dimensions since they shrink from the free ends [31], it would be a low pass filter. Experiments on oscillations in cells of the salivary gland of blowfly by Zimmermann *et al* [103] very much support this notion. In those experiments, mitochondria were also energized by pyruvate/malate. That reduced the frequency of oscillations by a factor of 2–3 and increased their amplitude. Evidence for the reduction of frequency by mitochondria has been found in oocytes as well. Marchant *et al* [67] measured the puff frequency of release sites in dependence on the number and proximity of surrounding mitochondria. They found that puff sites surrounded by larger mitochondrial mass or situated less than 1.25 μm away from mitochondria exhibit puff frequencies on average 1.7

times smaller than puff sites further away from mitochondria. In each imaging frame the fastest site far away from mitochondria was on average six times faster than the slowest puff site close to mitochondria. Remarkably, the amplitude of puffs was not influenced by mitochondria [67]. These data demonstrate that mitochondria even reduce frequencies of elemental events and without being energized, if they are close enough to the release site.

Mitochondrial Ca^{2+} fluxes modulate cytosolic Ca^{2+} transients. One action of mitochondria is a buffer-like reduction of amplitudes of cytosolic Ca^{2+} spikes and wave velocities [15, 22, 68]. Another characteristic effect on cytosolic Ca^{2+} signals is the appearance of biphasic decay of cytosolic Ca^{2+} spikes [5, 16, 75, 79, 88, 93]. Mitochondrial efflux slows down the decrease of cytosolic Ca^{2+} as soon as mitochondrial release becomes faster than uptake through the uniporter [16]. The effect may even lead to a plateau phase of cytosolic Ca^{2+} concentration, if mitochondrial release compensates almost completely for all other fluxes removing Ca^{2+} from the cytosol. The dispersion gap is the manifestation of this slowing down of the decay of cytosolic transients by mitochondria in wave characteristics, since it is caused by release of Ca^{2+} in the back of a wave. Abortion of wave propagation due to the buffer features of mitochondria occurs at even higher values of mitochondrial uptake.

2. Stochastic simulations

The existence of spontaneous wave creation by pacemakers with long periods is crucial for the explanation of the pattern formation with energized mitochondria given above. It can be explained by stochastic models which we will consider now. However, this is not the only question motivating research. Rather, in certain cells the question for the origin of long periods in general is of interest. For instance in Xenopus oocytes, wave periods of up to 120 s are observed, but the longest timescale of the channel dynamics is only about 10–15 s. Hence, the long periods cannot be explained by the local dynamics in Xenopus oocytes. One possibility to prolong Ca^{2+} oscillation periods is coupling to a phosphorylation–dephosphorylation cycle or receptor phosphorylation [35, 53]. However, this is probably not the case in Xenopus oocytes. Influx across the plasma membrane does not seem to set the period either, since dynamics on the timescale of a period is not very sensitive to the Ca^{2+} concentration in the extracellular medium in Xenopus oocytes [12, 47].

Regardless of these considerations, the best reason for stochastic models is the observation of stochastic phenomena in intracellular Ca^{2+} dynamics, the most prominent of which are the small localized release events called puffs. Puffs are the elemental events which are used to build up global events like waves and oscillations. Parker *et al* investigated this hierarchy of spatio-temporal structures in detail in Xenopus oocytes and Bootman *et al* in HeLa cells [7, 8, 10, 65, 66, 92, 97]. Typically, a single puff is not enough to initiate a wave [65]. Rather, the cooperative action of several puff sites is required. The mechanism by which waves are initiated following a step increase of IP_3 is not an increase in puff amplitude. The amplitude of puffs immediately preceding wave initiation was constant. The way the critical amount of Ca^{2+} is raised is an increasing puff frequency by up to a factor 10 [65]. Wave initiation has been investigated for periodic waves as well [66]. Measurements demonstrate typical differences between repetitive wave initiation with short and long periods. The peak of the previous wave was chosen as the reference time in the presentation of the results of the experiments [66]. Puffs did not occur in the first 7 s after a wave passed. Then, puffs occurred with increasing frequency. That increase continued till initiation of the next wave for short-period waves ($<$15 s). The puff

Table 2. Parameters for stochastic simulations. The first figure in column 'Value' refers to figures 12–17, the second one to figures 18 and 19. The simulations shown in the latter ones used constant lumenal concentrations and the fast buffer approximation [46] so that buffer rate constants do not appear in the equations. Parameters not occurring in a model are marked by '—'.

Parameter	Value	Unit
Leak flux coefficient P_l	0.0025, 10^{-4}	s^{-1}
Channel flux coefficient P	600; 3555	s^{-1}
Single channel radius R_s	0.0354; 0.01	μm
Cluster spacing outside focal sites	4.33; 3.5	μm
Maximum number of channels per cluster N_K^{max}	25; 27	
Number of additional clusters in focal sites N_F	5; 0	
Pump flux coefficient P_p	40; 80	$\mu M\ s^{-1}$
Pump dissociation constant K_d	0.2; 0.1	μM
Volume ratio V_{cyt}/V_{ER}	10.0; 5.4	
Concentration of free Ca^{2+} E in the ER	—; 6.75	μM
Diffusion coefficient D of free cytosolic Ca^{2+}	223; 223	$\mu m^2\ s^{-1}$
Diffusion coefficient D_E of free lumenal Ca^{2+}	40; —	$\mu m^2\ s^{-1}$
Diffusion coefficient D_m of cytosolic endogenous mobile buffer	11.26; 11.26	$\mu m^2\ s^{-1}$
Diffusion coefficient D_{ex} of cytosolic exogenous buffer	32.0; 32.0	$\mu m^2\ s^{-1}$
Diffusion coefficient D_{Em} for lumenal mobile buffer	1; —	$\mu m^2\ s^{-1}$
On-rates of fast buffers: $k_s^+, k_m^+, k_{ex}^+, k_{Es}^+, k_{Em}^+$	500; —	$(\mu M\ s)^{-1}$
Dissociation constants of buffers k_i^-/k_i^+:		
K_s	2; 9	μM
K_m	2; 6.72	μM
K_{ex}	0.247; 0.247	μM
K_{Es}	500; —	μM
K_{Em}	5; —	μM
Total concentrations of buffers:		
B_s	200; 95.31	μM
B_m	50; 19.1	μM
B_{ex}	60; 40	μM
B_{Es}	100; —	mM
B_{Em}	5; —	mM
Total concentration of Ca^{2+} C_0	5.385; —	mM
Subunit kinetics, note $b_i = a_i d_i, i = 1, \ldots, 5$		
a_2, a_4	0.0555; 0.2	$(\mu M\ s)^{-1}$
a_5	2.222; 20	$(\mu M\ s)^{-1}$
d_1	0.13; 0.13	μM
d_2	3.776; 1.049	μM
d_3	0.943; 0.953	μM
d_4	0.5202; 0.144	μM
d_5	0.72; 0.0823	μM
IP_3 concentration I	0.15	μM
a_6 (see figure 12)	$\frac{a_2 I + a_4 d_1}{d_1 + I}$	
b_6 (see figure 12)	$\frac{b_2 I + b_4 d_3}{d_3 + I}$	

amplitude quickly reached a certain level which then stayed constant for the last 30–40% of the wave period. Waves with intermediate periods (15–50 s) exhibit an increase in puff frequency from 7 s after the previous wave until about three-quarters of the way through the cycle. The amplitude again soon reaches its steady level which it then keeps for most (≈60%) of the cycle. Finally, waves with periods longer than 50 s did not show any essential variation in puff amplitude or puff frequency during the 60% of the wave cycle preceding the next wave [66].

Especially for long-period waves, the nucleation of a wave by the cooperative action of a few puffs can be demonstrated [65]. Since puffs are stochastic events, the formation of a supercritical nucleus occurs only with a certain probability. Marchant *et al* [66] state that the time elapsing between two consecutive waves is determined by two processes: the recovery from inhibition caused by the first wave and the creation of a supercritical nucleus for the second wave. The probabilistic character of nucleation introduces variability into the wave period. Marchant *et al* [66] report a standard deviation of up to 40% for long-period waves. That supports the interpretation of long-period repetitive waves as nucleation phenomena.

2.1. Stochastic channel models

The processes causing random behaviour in intracellular Ca^{2+} dynamics are the transitions between the different states of the channel subunits and the channel. Channels open and close randomly. The opening and closing probability depends on the state of the channel subunits. The opening probability is the highest, if a minimum number of subunits are activated.

The Othmer–Tang model reproduces the basic findings on IP_3 receptor channel dynamics. However, it does not consider certain details of regulation of the IP_3R by Ca^{2+} and IP_3, as e.g. the number of Ca^{2+} ions which need to bind for channel opening to occur. That might become relevant in stochastic simulations dealing with single binding and dissociation events. Hence, we use a more detailed model from now on. The model by DeYoung and Keizer was set up as a deterministic model by the authors [19] and used later on as a stochastic scheme by Falcke *et al* [28, 32]. The model assumes identical, independent subunits. Each subunit has three binding sites: an activating binding site, an inhibiting binding site and a binding site for IP_3. Subunits are activated, if IP_3 is bound, Ca^{2+} is bound to the activating site and is not bound to the inhibiting site. The channel is activated, if at least three subunits are activated. The stochastic events are binding of Ca^{2+} and IP_3 to and dissociation from the channel subunits.

We can simplify the model by taking advantage of the timescale separation between IP_3 binding and dissociation on one side and Ca^{2+} binding and dissociation on the other. DeYoung and Keizer assumed the IP_3 processes to be two orders of magnitude faster than the other reaction rates. That implies that the binding state of IP_3 will be in a stationary distribution most of the time and pairs of states with identical Ca^{2+} binding configuration can be lumped into one state. That leaves four lumped states of a subunit corresponding to Ca^{2+} bound or not bound to the activating and inhibiting binding sites. Given one of these four states, the subunit is in one of the substates of IP_3 binding with the probability given by the stationary distribution. Such a four-state scheme is shown in figure 12. The probability for transitions corresponding to binding of Ca^{2+} ions depends on the concentration of free Ca^{2+} at the location of the channel.

2.2. Modelling concentrations

The Ca^{2+} in a cell is transported through channels and by pumps, diffuses in the cytosol and the ER and reacts with buffers. These processes are described by reaction diffusion equations for the

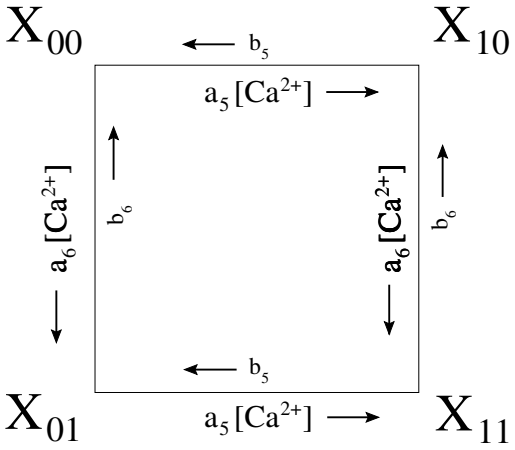

Figure 12. The four Ca^{2+} binding states X_{ik} of a subunit in the DeYoung–Keizer model. The index i corresponds to the activating site and k to the inhibiting site. An index is 1 if the site has an ion bound and 0 otherwise.

cytosolic concentration of free Ca^{2+} c, the concentration in the ER E and the buffer concentrations (with Ca^{2+} bound) in the cytosol and ER b_i and $b_{E,j}$. The buffer dynamics is binding and dissociation of Ca^{2+} and diffusion. The index 'i' of the buffer variable denotes different buffers like endogenous stationary buffer (s), endogenous mobile buffer (m) and exogenous mobile buffer (ex). Stationary buffers do not diffuse.

Living cells and their subcompartments are of course spatially three-dimensional objects. Nevertheless, the reaction diffusion problem is often reduced to two spatial dimensions. The fluxes between the compartments cytosol and ER are then scaled by the volume ratio $\gamma = V_{\text{cytosol}}/V_{\text{ER}}$. That leads to the partial differential equations

$$\begin{aligned}
\frac{\partial c}{\partial t} &= D\nabla^2 c + (P_\text{l} + P_\text{c}(r,t))(E-c) - P_\text{p}\frac{c^2}{K_\text{d}^2 + c^2} - H_i(c, b_i) \\
\frac{\partial E}{\partial t} &= D_E\nabla^2 E - \gamma\left[(P_\text{l} + P_\text{c}(r,t))(E-c) - P_\text{p}\frac{c^2}{K_{\text{d}^2} + c^2}\right] - H_j(E, b_{E,j}) \\
\frac{\partial b_i}{\partial t} &= H_i(c, b_i) = D_{\text{b},i}\nabla^2 b_i + k_\text{b}^+(B_i - b_i)c - k_{\text{b},i}^- b_i, \qquad i = \text{s, ex, m} \\
\frac{\partial b_{E,j}}{\partial t} &= H_j(E, b_{E,j}) = D_{E,j}\nabla^2 b_{E,j} + k_{E,j}^+(G_i - b_{E,j})E - k_{E,j}^- b_{E,j}, \qquad j = \text{s, m.}
\end{aligned} \tag{2}$$

The first term in the equation for the cytosolic Ca^{2+} concentration c is the diffusion term. The second and third terms model the Ca^{2+} flux through the membrane of the ER. P_l is the coefficient for a leak flux proportional to the concentration difference $E - c$. The function $P_\text{c}(r, t)$ describes the location and opening state of channel clusters. $P_\text{c}(r, t)$ has a positive value P at the location of a cluster, if channels in the cluster are open. We include the number of open channels by the size of the area where $P_\text{c}(r, t)$ is larger than zero. That area equals $N_\text{o}R_\text{S}^2$. R_S is a radius reflecting the spacing of channels within a cluster and N_o is the number of open channels. The third term of the equation for c (P_p) models the action of the pumps transporting Ca^{2+} from the cytosol into the ER. We describe that as a spatially continuous flux density depending on c. The last term of the equation describes the reaction of free Ca^{2+} with buffers. The equation for the

dynamics of the lumenal concentration E includes diffusion, the flux through the membrane and the reaction with lumenal buffers. The flux terms are those appearing as well in the equation for cytosolic Ca^{2+} only with opposite sign and scaled by the volume ratio γ. The last two equations describe the dynamics of the buffers with Ca^{2+} bound. The first term is the buffer diffusion, and the second term the binding of Ca^{2+} to the free buffer represented as the difference between the (constant) total concentration and the concentration of Ca^{2+}-bound buffer, e.g. $(B_i - b_i)$. The last term of buffer dynamics is the rate of Ca^{2+} dissociation from the buffer.

When a channel opens, a concentration profile builds up quickly in the cytosol and inside the ER. A stationary state is reached when free Ca^{2+} has spread far enough so that removal of Ca^{2+} from the cytosol back into the ER balances the flux through the channel.

In order to reach a simulation procedure able to simulate long timescales and large length scales adiabatic approximations were applied [27, 28]. The crucial approximation was to replace the time-dependent formation of the concentration profile around a cluster by the stationary solution belonging to the actual number of open channels. This is well justified for the concentrations at the location of the cluster but meaningful on the length scale of cluster spacing too as explained in [28]. Basically, this is based on the localization of the profiles by buffers which reduce the diffusion length by binding free Ca^{2+}.

Buffers localize concentration profiles so strongly that the concentration increase due to open channels is about two orders of magnitude smaller at the next neighbour's location than at the cluster with open channels itself. The localization can be used to further simplify simulations. The increase due to release through open channels is the difference between the base level concentrations (when all channels are closed) and the concentration profile (when channels are open) and we call it single-cluster profile. It approaches 0 for large distances from the cluster. In taking advantage of the localization of single-cluster profiles, the complete concentration field can be represented as sum of the base level and a superposition of all single-cluster profiles.

The single-cluster concentration profiles for all possible numbers of open channels can be calculated in advance to the simulation. During the simulation, we appoint a single-cluster profile to a cluster according to its number of open channels. The superposition of all profiles is the global concentration field [28]. The concentration fields and the cluster dynamics are mutually coupled. On the one hand, the transition rates for binding transitions depend on the concentration of free Ca^{2+} as shown in figure 12. On the other hand, the concentration fields depend on the configuration of open channels.

2.3. Stochastic wave patterns

Stochastic simulations comprising up to 712 clusters were performed on a cluster array like that shown in figure 13. Clusters were arranged on a hexagonal grid with a few additional clusters scattered in between to mimic focal sites (see figure 13 for details). The number of channels in each cluster was drawn from a uniform distribution between $N_K^{\max}/2$ and $N_K^{\max}$.

A set of simulations for different IP_3 concentrations is shown in figure 14. Only puffs are found at low concentrations, i.e. release events are localized and not coordinated on a length scale of several cluster distances. That changes with the onset of global events at a slightly higher IP_3 (figure 14(A)). These global events are waves emerging from a nucleation area. They are very rare for low IP_3 concentrations and may travel across the whole system (figure 14(A), first and second peak) or fade away before they reach the system boundary (third peak). That parameter regime of abortive wave propagation is characterized by a distribution of the probability for

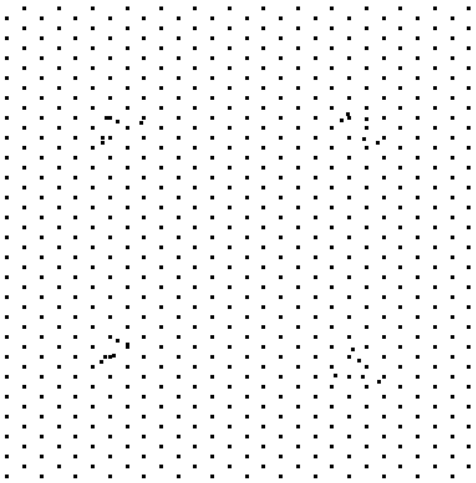

Figure 13. Array of clusters used in simulations. The area is quadratic with edge length $L = 120\ \mu$m. Clusters form a hexagonal grid with distance d. N_F further clusters are scattered randomly around the points $(L/4, L/4)$, $(L/4, 3L/4)$, $(3L/4, L/4)$, $(3L/4, 3L/4)$ within a square with edge length $2.42d$ mimicking a focal site; here $N_F = 5$.

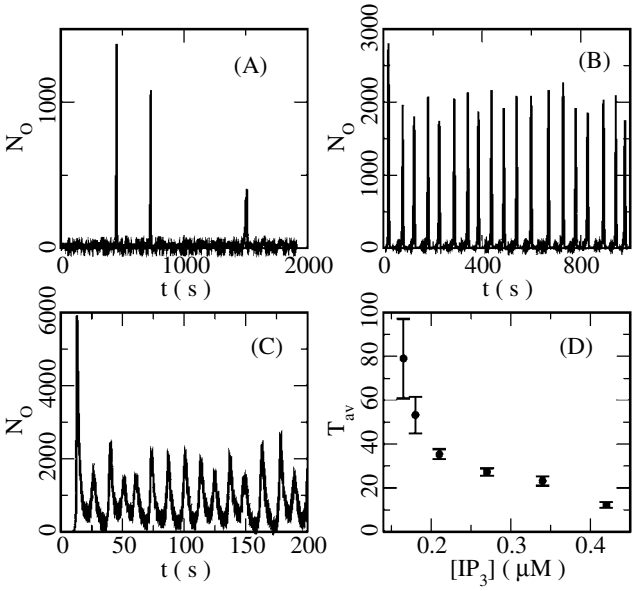

Figure 14. Simulations and oscillation characteristics for different IP_3 concentrations: (A) $I = 0.15\ \mu$M, (B) $I = 0.18\ \mu$M (see animation), (C) $I = 0.42\ \mu$M, (D) T_{av} and its standard deviation in dependence on IP_3. (Figure from [28].)

a wave to travel a certain distance before being destroyed by fluctuations rather than steadily propagating waves [32].

Increasing IP_3 leads to more frequent waves (figure 14(B)) and almost every wave travels across the whole system now. The time interval in between waves is not completely regular like the period of a deterministic oscillation, but an average interwave time interval T_{av} and its

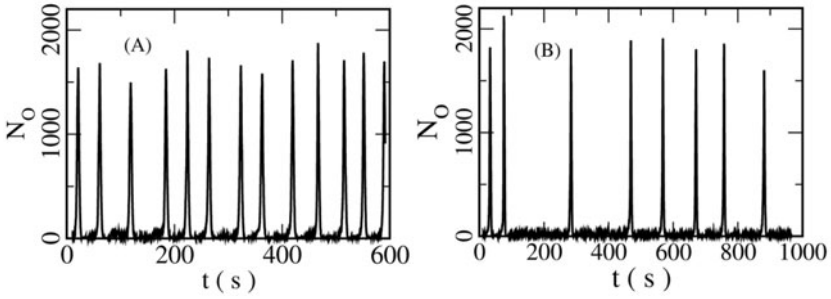

Figure 15. Repetitive wave nucleation for two concentrations of exogenous buffer: (A) $B_{ex} = 60\ \mu$M, (B) $B_{ex} = 75\ \mu$M. The number of open channels is shown. The average period in (A) is $T_{av} = 47.40 \pm 10.00$ s, and in (B) $T_{av} = 121.17 \pm 57.23$ s. The transition from $X_{01} \rightarrow X_{00}$ was increased by a factor of 2.5 compared to the standard parameters of table 1. See table 1 for further parameters except $N_F = 10$. (Figure from [28].)

standard deviation ΔT_{av} can be determined. Both T_{av} and ΔT_{av} decrease with increasing IP_3 (figure 14(D)) leading to almost regular oscillations with a period of about 17 s at high IP_3 (figure 14(C)). That scenario found while going from low to high IP_3 agrees with experimental observations [66]. In particular, the large range of periods of eight times the shortest one reported from the experiments is captured. Short periods can be set essentially by the longest timescale of the channel dynamics T_d being the transition to the inhibited state and recovery from it. However, long periods last 3–8 times longer and cannot be explained by the channel dynamics alone.

Long periods can be explained by wave nucleation. Waves emerge from small areas—a nucleus—and than spread through the whole system. Nucleation of global events is probabilistic, because a single puff activates a neighbouring cluster with a certain probability only—not with certainty. The nucleation probability p_n is small compared to the puff probability because a large supercritical nucleus of a few clusters is needed. The larger a nucleus, the smaller is the curvature of its boundary. The smaller the curvature of the boundary, the larger is the number of active neighbours of an inactive cluster just outside the nucleus and hence the probability that that cluster is activated. Hence, the larger the nucleus the larger is the probability that it grows. Deactivation, inhibition and fluctuations hinder the growth of a nucleus. In that way, a critical size of a nucleus arises.

The nucleation probability is very small just after a wave has travelled across the system because of inhibition of most of the channels by the high Ca^{2+} concentration during the wave. That causes the deterministic part T_d of the time elapsing between two consecutive waves. T_d is determined essentially by the transition rates from the activated state (X_{10}) to the inhibited state (X_{11}) and recovery from inhibition ($X_{11} \rightarrow X_{01} \rightarrow X_{00}$). However, p_n is still small after recovery from inhibition. Hence, the next wave does not emerge immediately but it takes some time before another global event can be set off. The small value of p_n provides for the larger part of T_{av} at low IP_3 [28].

The period increases with decreasing strength of spatial coupling and decreases with increasing system size in agreement with the idea of nucleation processes setting long periods [27, 28] (see figure 16). Average periods created by wave nucleation are in the range observed experimentally. The nontrivial information carried by the data is the good agreement between experimentally measured and simulated ratios of the standard deviation of periods to the

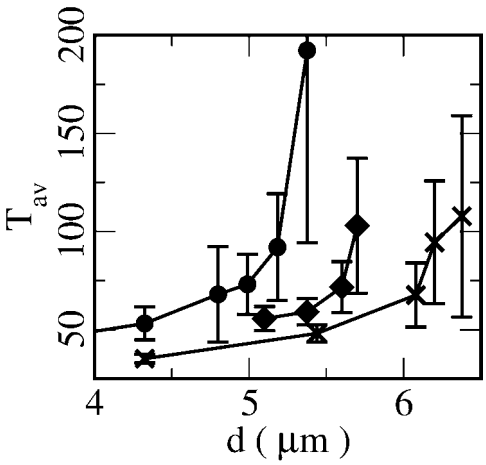

Figure 16. The average period T_{av} of repetitive wave nucleation and its standard deviation in dependence on the cluster spacing. See table 1 for further parameters except $N_F = 10$, $I = 0.10$ μM (circles), $N_F = 5$, $I = 0.195$ μM (diamonds) and $N_F = 5$, $I = 0.21$ μM ($\times$). (Figure from [28].)

average period $\Delta T_{av}/T_{av}$ (see [28]). That supports the nucleation hypothesis. Simulations with different random realizations of a cluster array with identical average cluster spacing and average number of channels per cluster showed differential T_{av} and a varying relative standard deviation $\Delta T_{av}/T_{av}$ as well. That implies that there are optimal arrays having minimal $\Delta T_{av}/T_{av}$ [28].

Oscillation periods were sensitive to changes in the number of channels per cluster and the strength of spatial coupling. In particular, the sensitivity for the average number of excitable channels per cluster raises the question for the deterministic limit. The deterministic limit assumes infinitely many channels per cluster while keeping the flux density and $N_K^{max} R_S^2$ constant. Simulations showed that T_{av} changes by a factor of 5 while going from 25 to 328 channels per cluster at low IP_3. Results with even higher values of N_K^{max} suggest that the deterministic limit is not oscillatory, but is a stationary state with high activity compared to the activity between waves during long-period oscillations (figure 17). That means that the oscillations are completely due to fluctuations, i.e. stochastic binding and dissociation of Ca^{2+}. Obviously, the fluctuations occurring with realistic channel numbers are large enough to leave the attractive region (stable manifold) of the high-activity stationary state, which is observed for channel numbers approaching the deterministic limit. We find again a high-activity stationary state for larger IP_3 and large N_K^{max} (figure 17, insets). That means that short-period oscillations with small N_K^{max}, too, are due to fluctuations.

The stationary high-activity state reflects the behaviour of the DeYoung–Keizer model. Such a state can be reached in the deterministic model by increasing the Ca^{2+} flux through channels, which causes an increase of the cytosolic Ca^{2+} concentration. That situation occurs at the location of open channels in a discrete model. The high local Ca^{2+} concentration suppresses oscillatory behaviour, which needs intermediate Ca^{2+} concentrations. That suggests that the oscillatory regime in models is lost during the transition from spatially continuous channel density to spatial discreteness of the channel clusters while keeping the average flux density constant. Fluctuations compensate for that by restoring the ability for oscillatory behaviour.

In the simulations presented up to now, we have found a strong dependence of pattern timescales on the number of channels per cluster. Such dependence exists for other characteristics

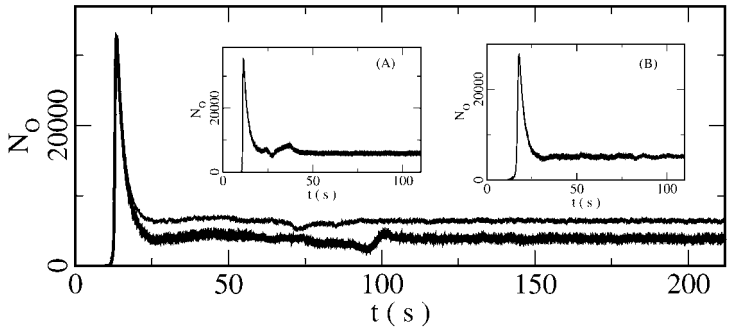

Figure 17. Simulations with $N_K^{\max} = 1130$, $I = 0.15\ \mu$M and $N_F = 5$. The single-channel radius was chosen proportional to $(N_K^{\max})^{-1/2}$ as explained in the text. The case shown corresponds to figure 14 (A) (thick curve) and with recovery from inhibition sped up by a factor of 2.5 (thin curve). Insets: simulations with (A) $I = 0.42\ \mu$M, $N_K^{\max} = 546$ and (B) $I = 0.27\ \mu$M, $N_K^{\max} = 685$. (Figure from [28].)

of patterns, too. We have merely to consider larger length scales in order to be able to observe it. Patterns on these large spatial scales are shown in figures 18 and 19. The spiral in the left panel of figure 18 was simulated with a larger number of channels per cluster than the right one, but again both systems have the same mean field equations. The difference in the wavelengths of the spirals is obvious. The spiral on the left-hand side rotates with a period of about 45 s and the one on the right-hand side with approximately 75 s. The transition to the deterministic limit is demonstrated in figure 19 on the basis of spatio-temporal patterns. Pulses forming more or less stable spirals are observed at small numbers of channels per clusters. At large numbers, front waves occur. They are the trademark pattern of bistable local dynamics. The bistability disappears in a saddle node bifurcation at very low IP_3. A very similar dependence of wavelength and periods on noise strength was found by Jung and Mayer-Kress [50] in a two-dimensional array of pulse coupled threshold elements.

3. Concluding remarks

Intracellular Ca^{2+} dynamics exhibits a duality of stochastic and deterministic features. Puffs are clearly stochastic events. Stochasticity shows up in global events as well in the form of period distributions instead of regular oscillations and as the wave creation mechanism [27, 28, 32, 66]. The smooth wavefronts observed in experiment (figure 1) and in stochastic simulations (figure 19) suggest that a deterministic description should be possible whereas the strong dependence of wave characteristics on channel numbers contradicts that assumption. Langevin equations like those used by Shuai *et al* [49, 85, 86] for single-cluster models are suggested by the observations in simulations. However, they fail at the small numbers of channels per cluster which occur in the wave nucleation regime.

The results of deterministic and stochastic modelling complement one another. Deterministic models allow the understanding of wave propagation with the theory of nonlinear partial differential equations and of wave instabilities with bifurcation theory. Stochastic descriptions explain local spontaneous events and the generation of waves. In the course of the research on wave instabilities with energized mitochondria, bistability was suggested by theory and confirmed experimentally by the observation of fronts figure 7. It was assumed in

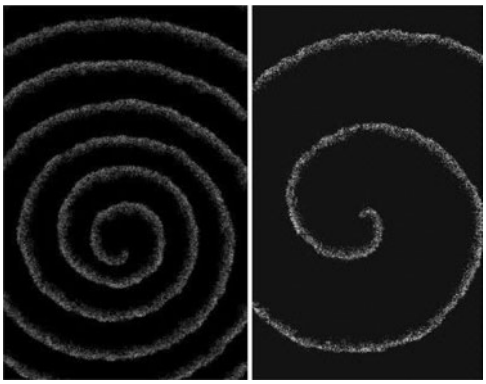

Figure 18. Simulations with different $N_K^{\max}$ but the same deterministic limit. The single-channel radius was chosen proportional to $(N_K^{\max})^{-1/2}$ as explained in the text. Left panel, $N_K^{\max} = 60$ (see animation); right panel, $N_K^{\max} = 27$ (see animation). The size of the simulation area is 1.31×1.57 mm^2, $I = 0.100$ μM. See table 1 for further parameters.

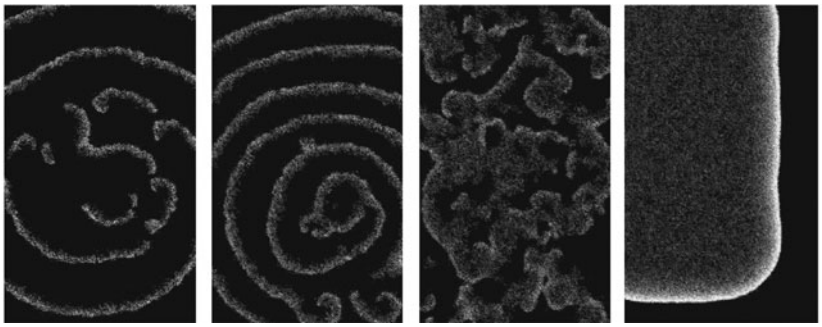

Figure 19. Simulations with different $N_K^{\max}$ but the same deterministic limit. The single-channel radius was chosen proportional to $(N_K^{\max})^{-1/2}$ as explained in the text. $N_K^{\max}$ from left to right 23 (animation a), 35 (animation b), 47 (animation c), 71 (animation d). For all panels $I = 0.175$ μM, concentration of free Ca^{2+} in the ER $E = 3.375$ μM, $P = 3614$ s^{-1}, $P_p = 40$ μM s^{-1}. The size of the simulation area is 1.31×1.57 mm^2. See table 1 for further parameters.

the model for the fertilization wave in Xenopus oocytes as well [100]. An explanation of long timescales in Xenopus oocytes and slow pacemakers was suggested by stochastic modelling. Simulations with large numbers of channels per cluster suggest bistability as the deterministic limit of the stochastic system too (see figure 17). In both systems, pulses—a wave type more typical for excitable or oscillatory dynamic regimes—were found in a bistable regime. Pulses coexist in the deterministic model with fronts. They are due to fluctuations around the higher stationary state, which push the system out of the basin of attraction, in the stochastic model.

The most obvious drawback of the stochastic approach is that it introduces a new parameter which is the number of channels per cluster. Sun *et al* [92] obtained an estimate of maximal 8 open channels per cluster during a puff. That is close to the estimate by Mak *et al* of 5 [62] and leads to 15–30 channels per cluster taking the IP_3 binding probability into account. However, these numbers are based on single-channel current estimates which are not known very precisely.

The stochastic simulations presented here and in [27, 28, 32] suggest that the concept of excitable, bistable or oscillatory dynamic regimes of ordinary differential equations or partial differential equations might be of limited use applied to intracellular Ca^{2+} dynamics. That is supported by the results of Shuai and Jung [49, 85, 86]. They found that a Hopf bifurcation of the deterministic limit of a single-cluster model does not show up in the stochastic puff behaviour. The concept of thresholds separating perturbations which decay from those which are amplified might turn out to be useful for comprehending nucleation phenomena and the transition from long- to short-period oscillations [28]. However, at the current state of research, neither the existence of oscillations nor the wave type can be reliably predicted from just the type of deterministic regime.

Nucleation could be found for a variety of parameters of the local dynamics [28]. One parameter the global behaviour of intracellular Ca^{2+} dynamics is very sensitive to is the number of channels per cluster which can be activated by Ca^{2+}. That number is controlled by IP_3. In summary, the picture arises that nature created a robust stochastic mechanism that does not much care about dynamic regimes but can easily be controlled by the IP_3 concentration.

Parameters like spatial coupling and the number of channels, which can be activated by Ca^{2+}, can be tuned experimentally. Hence, the experimental access as a prerequisite for fruitful research is given. Given the value and success of both approaches, the relation between stochastic and deterministic features and models of intracellular Ca^{2+} dynamics will be a major issue of this research.

References

[1] Alberts B, Bray D, Lewis J, Raff M, Roberts K and Watson J D 1994 *Molecular Biology of the Cell* 3rd edn (New York: Garland)

[2] Applegate T L, Karjalainen A and Bygrave F L 1997 Rapid Ca^{2+} influx by the action of dibutylhydroquinone and glucagon in the perfused rat liver *Biochem. J.* **323** 463–7

[3] Atri A, Amundson J, Clapham D and Sneyd J 1993 A single pool model for intracellular calcium oscillations and waves in the Xenopus laevis oocyte *Biophys. J.* **65** 1727–39

[4] Babcock D F, Herrington J, Goodwin P C, Park Y B and Hille B 1997 Mitochondrial participation in the intracellular Ca^{2+} network *J. Cell Biol.* **136** 833–44

[5] Babcock D F and Hille B 1998 Mitochondrial oversight of cellular Ca^{2+} signals *Curr. Opin. Neurobiol.* **8** 398–404

[6] Berridge M J, Bootman M D and Lipp P 1998 Calcium—a life and death signal *Nature* **395** 645–8

[7] Bootman M, Berridge M and Lipp P 1997 Cooking with calcium: the recipes for composing global signals from elementary events *Cell* **91** 367–73

[8] Bootman M, Niggli E, Berridge M and Lipp P 1997 Imaging the hierarchical Ca^{2+} signalling in HeLa cells *J. Physiol.* **499** 307–14

[9] Budd S L and Nicholls D G 1996 A reevaluation of the role of mitochondria in neuronal Ca^{2+} homeostasis *J. Neurochem.* **66** 403–11

[10] Callamaras N, Marchant J S, Sun X-P and Parker I 1998 Activation and co-ordination of $InsP_3$-mediated elementary Ca^{2+} events during global Ca^{2+} signals in Xenopus oocytes *J. Physiol.* **509** 81–91

[11] Callamaras N and Parker I 2000 Phasic characteristics of elementary Ca^{2+} release sites underlies quantal responses to IP_3 *EMBO J.* **19** 3608–17

[12] Camacho P and Lechleiter J D 1993 Increased frequency of calcium waves in Xenopus laevis oocytes that express a calcium-atpase *Science* **260** 226–9

[13] Camacho P and Lechleiter J D 1995 Spiral calcium waves: implications for signalling *Calcium Waves, Gradients and Oscillations (Ciba F Symposium vol 188)* (Chichester: Wiley)

[14] Cheek T R, Berridge M J, Moreton R B, Stauderman K A, Murawsky N M and Bootman M D 1994 Quantal Ca^{2+} mobilization by ryanodine receptors is due to all-or-none release from functionally discrete intracellular stores *Biochem. J.* **301** 879–83
[15] Colegrove S L, Albrecht M A and Friel D D 2000 Direction of mitochondrial Ca^{2+} uptake and release fluxes *in situ* after depolarization-evoked $[Ca^{2+}]_i$ elevations in sympathetic neurons *J. Gen. Physiol.* **112** 351–69
[16] Colegrove S L, Albrecht M A and Friel D D 2000 Quantitative analysis of mitochondrial Ca^{2+} uptake and release pathways in sympathetic neurons *J. Gen. Physiol.* **112** 371–88
[17] Csordás G, Thomas A P and Hajnóczky G 1999 Quasi synaptic calcium signal transmission between endoplasmic reticulum and mitochondria *EMBO J.* **18** 96–108
[18] D'Andrea P and Vittur F 1995 Spatial and temporal Ca^{2+} signalling in articular chondrocytes *Biochem. Biophys. Res. Commun.* **75** 129–35
[19] DeYoung G W and Keizer J 1992 A single-pool inositol 1,4,5-trisphosphate-receptor-based model for agonist-stimulated oscillations in Ca^{2+} concentration *Proc. Natl Acad. Sci. USA* **89** 9895–9
[20] Drummond R M and Fay F S 1996 Mitochondria contribute to Ca^{2+} removal in smooth muscle cells *Pflügers Arch.* **431** 473–82
[21] Drummond R M and Tuft R A 1999 Release of Ca^{2+} from the sarcoplasmic reticulum increases mitochondrial $[Ca^{2+}]$ in rat pulmonary artery smooth muscle cells *J. Physiol.* **516** 139–47
[22] Duchen M R 2000 Mitochondria and Ca^{2+} in cell physiology and pathophysiology *Cell Calcium* **28** 339–48
[23] Dupont G 1998 Theoretical insights into the mechanism of spiral Ca^{2+} wave initiation in Xenopus oocytes *Am. J. Physiol.* **275** C317–22
[24] Dupont G and Goldbeter A 1993 One-pool model for Ca^{2+} oscillations involving Ca^{2+} and inositol 1,4,5-trisphosphate as co-agonists for Ca^{2+} release *Cell Calcium* **14** 311–22
[25] Dupont G and Goldbeter A 1994 Properties of intracellular Ca^{2+} waves generated by a model based on Ca^{2+}-induced Ca^{2+} release *Biophys. J.* **67** 2191–204
[26] Dupont G and Swillens S 1995 Quantal release, incremental detection, and long-period Ca^{2+} oscillations in a model based on regulatory Ca^{2+}-binding sites along the permeation pathway *Biophys. J.* **71** 1714–22
[27] Falcke M 2003 Buffers and oscillations in intracellular Ca^{2+} dynamics *Biophys. J.* **84** 28–41
[28] Falcke M 2003 On the role of stochastic channel behavior in intracellular Ca^{2+} dynamics *Biophys. J.* **84** 42–56
[29] Falcke M, Bär M, Lechleiter J D and Hudson J L 1999 Spiral breakup and defect dynamics in a model for intracellular Ca^{2+} dynamics *Physica* D **129** 236–52
[30] Falcke M, Hudson J L, Camacho P and Lechleiter J D 1999 Impact of mitochondrial Ca^{2+} cycling on pattern formation and stability *Biophys. J.* **77** 37–44
[31] Falcke M, Or-Guil M and Bär M 2000 Dispersion gap and localized spiral waves in a model for intracellular Ca^{2+} dynamics *Phys. Rev. Lett.* **84** 4753–6
[32] Falcke M, Tsimring L and Levine H 2000 Stochastic spreading of intracellular Ca^{2+} release *Phys. Rev.* E **62** 2636–43
[33] Fontanilla R A and Nuccitelli R 1998 Characterization of the sperm-induced calcium wave in Xenopus eggs using confocal microscopy *Biophys. J.* **75** 2079–87
[34] Friel D D 2000 Mitochondria as regulators of stimulus-evoked calcium signals in neurons *Cell Calcium* **28** 307–16
[35] Gall D, Baus E and Dupont G 2000 Activation of the liver glycogen phosphorylase by Ca^{2+} oscillations: a theoretical study *J. Theor. Biol.* **207** 445–54
[36] Golovina V A and Blaustein M P 1997 Spatially and functionally distinct Ca^{2+} stores in sarcoplasmic and endoplasmic reticulum *Science* **275** 1643–8
[37] Gu X and Spitzer N 1995 Distinct aspects of neuronal differentiation encoded by frequency of spontaneous Ca^{2+} transients *Nature* **375** 784–7
[38] Gunter T E, Buntinas L, Sparagna G C and Gunter K K 1998 The Ca^{2+} transport mechanism of mitochondria and Ca^{2+} uptake from physiological-type Ca^{2+} transients *Biochim. Biophys. Acta* **1366** 5–15

[39] Gunter T E and Pfeiffer D R 1990 Mechanism by which mitochondria transport calcium *Am. J. Physiol.* **258** C755–86
[40] Gurney A M, Drummond R M and Fay F S 2000 Calcium signalling in sarcoplasmic reticulum, cytoplasm and mitochondria during activation of rabbit aorta myocytes *Cell Calcium* **27** 339–51
[41] Haak L L, Grimaldi M and Russel J T 2000 Mitochondria in myelinating cells: calcium signaling in oligodendrocyte precursor cells *Cell Calcium* **28** 297–306
[42] Hajnóczky G, Hager R and Thomas A P 1999 Mitochondria suppress local feedback activation of Inositol 1,4,5-trisphosphate receptors by Ca^{2+} *J. Biol. Chem.* **274** 14157–62
[43] Hajnóczky G and Thomas A P 1997 Minimal requirements for calcium oscillations driven by the IP_3 receptor *EMBO J.* **16** 3533–43
[44] Hannaert-Merah Z, Coquil J-F, Combettes L, Claret M, Mauger J-P and Champeil P 1994 Rapid kinetics of myo-Inositol trisphosphate binding and dissociation in cerebellar microsomes *J. Biol. Chem.* **269** 29642–9
[45] Ichas F, Jouaville L S, Sidah S S, Mazat J-P and Holmuhamedov E L 1994 Mitochondrial calcium spiking: a transduction mechanism based on calcium-induced permeability transition involved in cell calcium signalling *FEBS Lett.* **348** 211
[46] Jafri M S and Keizer J 1995 On the roles of Ca^{2+} diffusion, Ca^{2+} buffers and the endoplasmatic reticulum in IP_3-induced Ca^{2+} waves *Biophys. J.* **69** 2139–53
[47] Jafri M S, Vajda S and Gillo B 1992 A membrane model for cytosolic calcium oscillations. A study using Xenopus oocytes *Biophys. J.* **63** 235–46
[48] Jouaville L S, Ichas F, Holmuhamedov E L, Camacho P and Lechleiter J D 1995 Synchronisation of calcium waves of mitochondrial substrates in Xenopus laevis oocytes *Nature* **377** 438–41
[49] Jung P and Galley P C 2000 The heartbeat of extended clocks *Ann. Phys., NY* **9** 697–704
[50] Jung P and Mayer-Kress G 1994 Noise controlled spiral growth in excitable media *Chaos* **5** 458–62
[51] Kandel E R, Schwartz J H and Jessel T M 1991 *Principles of Neural Science* (Norwalk, CT: Appleton and Lange)
[52] Keizer J and Smith G D 1998 Spark-to-wave transition: saltatory transmission of calcium waves in cardiac myocytes *Biophys. Chem.* **72** 87–100
[53] LeBeau A, Yule D I, Groblewski G E and Sneyd J 1999 Agonist-dependent phosphorylation of the inositol 1,4,5-trisphosphate receptor—a possible mechanism for agonist-specific calcium oscillations in pancreatic acinar cells *J. Gen. Physiol.* **113** 851–71
[54] Lechleiter J D and Clapham D 1992 Molecular mechanism of intracellular calcium excitability in Xenopus laevis oocytes *Cell* **69** 283–94
[55] Lechleiter J D, Girard S, Clapham D and Peralta E 1991 Subcellular patterns of calcium release determined by g-protein-specific residues of muscarinic receptors *Nature* **350** 505–8
[56] Lechleiter J D, John L M and Camacho P 1998 Ca^{2+} wave dispersion and spiral wave entrainment in Xenopus laevis oocytes overexpressing Ca^{2+} atpases *J. Biophys. Chem.* **72** 123–9
[57] Lechleiter J D, Girard S, Peralta E and Clapham D 1991 Spiral calcium wave propagation and annihilation in Xenopus laevis oocytes *Science* **252** 123–6
[58] Lytton J, Westlin M, Burk S E, Shull G E and MacLennan D H 1992 Functional comparisons between isoforms of the sarcoplasmic or endoplasmic reticulum family of calcium pumps *J. Biol. Chem.* **267** 14483–9
[59] Magnus G and Keizer J 1997 Minimal model of β-cell mitochondrial Ca^{2+} handling *Am. J. Physiol.* **273** C717–33
[60] Magnus G and Keizer J 1998 Model of β-cell mitochondrial calcium handling and electrical activity: I. Cytoplasmic variables *Am. J. Physiol.* **274** C1158–73
[61] Magnus G and Keizer J 1998 Model of β-cell mitochondrial calcium handling and electrical activity: II. Mitochondrial variables *Am. J. Physiol.* **274** C1173–84
[62] Mak D D and Foskett J K 1997 Single-channel kinetics, inactivation, and spatial distribution of inositol trisphophate (IP_3) receptor in Xenopus oocyte nucleus *J. Gen. Physiol.* **109** 571–87

[63] Mak D D and Foskett J K 1998 Effects of divalent cations on single-channel conduction properties of Xenopus IP_3 receptor *Am. J. Physiol.* **275**
[64] Mak D D, McBride S, Raghuram V, Yue Y, Joseph S K and Foskett J K 2000 Single-channel properties in endoplasmic reticulum membrane of recombinant type 3 inositol trisphosphate receptor *J. Gen. Physiol.* **115** 241–55
[65] Marchant J, Callamaras N and Parker I 1999 Initiation of IP_3-mediated Ca^{2+} waves in Xenopus oocytes *EMBO J.* **18** 5285–99
[66] Marchant J S and Parker I 2001 Role of elementary Ca^{2+} puffs in generating repetitive Ca^{2+} oscillations *EMBO J.* **20** 65–76
[67] Marchant J S, Ramos V and Parker I 2002 Structural and functional relationships between Ca^{2+} puffs and mitochondria in Xenopus oocytes *Am. J. Physiol.* **282** C1374–86
[68] Marhl M, Schuster St and Brumen M 1998 Mitochondria as an important factor in the maintenance of constant amplitudes of cytosolic calcium oscillations *Biophys. Chem.* **71** 125–32
[69] Missiaen L, Taylor C W and Berridge M J 1991 Spontaneous calcium release from inositol trisphosphate sensitive calcium stores *Nature* **352** 241–4
[70] Nathanson H M, Burgstahler A D and Fallon M B 1994 Multistep mechanism of polarized Ca^{2+} wave patterns in hepatocytes *Am. J. Physiol.* **267** G338–49
[71] Nuccitelli R 1991 How do sperm activate eggs? *Curr. Top. Dev. Biol.* **25** 1–16
[72] Orchard C H, Mustafa M R and White K 1995 Oscillations and waves of intracellular [Ca^{2+}] in cardiac muscle cells *Chaos Solitons Fractals* **5** 447–58
[73] Parys J B, Missiaen L, DeSmedt H and Casteels R 1993 Loading dependence of inositol 1,4,5-trisphosphate-induced calcium release in the clonal cell line a7r5 *J. Biol. Chem.* **268** 25206–12
[74] Patel S, Joseph S K and Thomas A P 1999 Molecular properties of inositol 1,4,5-trisphosphate receptors *Cell Calcium* **25** 247–64
[75] Ricken S, Leipziger J, Greger R and Nitschke R 1998 Simultaneous measurements of cytosolic and mitochondrial Ca^{2+} transients in HT_{29} cells *J. Biol. Chem.* **273** 34961–9
[76] Ridgway E B, Gilkey J C and Jaffe L F 1977 Free calcium increases explosively in activating medaka eggs *Proc. Natl Acad. Sci. USA* **74** 623–7
[77] Rizzuto R, Bernardi P and Pozzan T 2000 Mitochondria as all-round players of the calcium game *J. Physiol.* **529** 37–47
[78] Rizzuto R, Brini M, Murgia M and Pozzan T 1993 Microdomains with high Ca^{2+} close to IP_3-sensitive channels that are sensed by neighboring mitochondria *Science* **262** 744–7
[79] Rizzuto R, Pinton P, Carrington W, Fay F S, Fogarty K E, Lifshitz L M, Tuft R A and Pozzan T 1998 Close contacts with the endoplasmic reticulum as determinants of mitochondrial Ca^{2+} responses *Science* **280** 1763–6
[80] Rizzuto R, Simpson A V M, Brini M and Pozzan T 1992 Rapid changes of mitochondrial calcium revealed by specifically targeted recombinant aequorin *Nature* **358** 325–7
[81] Robb-Gaspers L D, Burnett P, Rutter G A, Denton R M, Rizzuto R and Thomas A P 1998 Integrating cytosolic calcium signals into mitochondrial metabolic responses *EMBO J.* **17** 4987–5000
[82] Robb-Gaspers L D, Rutter G A, Burnett P, Hajnóczky G, Denton R M and Thomas A P 1998 Coupling between cytosolic and mitochondrial calcium oscillations: role in the regulation of hepatic metabolism *Biochim. Biophys. Acta* **1366** 17–32
[83] Satoh T, Ross C A, Villa A, Supattapone S, Pozzan T, Snyder S H and Meldolesi J 1990 The inositol 1,4,5-trisphosphate receptor in cerebellar Purkinje cells: quantitative immunogold labelling reveals concentration in an er subcompartment *J. Cell Biol.* **111** 615–24
[84] Selivanov V A, Ichas F, Holmuhamedov E L, Jouaville L S, Evtodienko Y V and Mazat J-P 1998 A model of mitochondrial Ca^{2+}-induced Ca^{2+} release simulating the Ca^{2+} oscillations and spikes generated by mitochondria *Biophys. Chem.* **72** 111–21
[85] Shuai J W and Jung P 2002 Optimal intracellular calcium signalling *Phys. Rev. Lett.* **88** 068102-1–4

[86] Shuai P and Jung P 2002 Stochastic properties of Ca^{2+} release of inositol 1,4,5-trisphosphate receptor clusters *Biophys. J.* **83** 87–97
[87] Sienaert I, DeSmet H, Parys J B, Missiaen L, Vanlingen S, Sipma H and Casteels R 1996 Characterization of a cytosolic and a luminal Ca^{2+} binding site in the type *i* inositol 1,4,5-trisphosphate receptor *J. Biol. Chem.* **271** 27005–12
[88] Simpson P B, Mehotra S, Langley D, Sheppard C A and Russell J T 1998 Specialized distributions of mitochondria and endoplasmic proteins define Ca^{2+} wave amplification sites in cultured astrocytes *J. Neurosci. Res.* **52** 672–83
[89] Sneyd J, Dale P D and Duffy A 1998 Traveling waves in buffered systems: applications to calcium waves *SIAM J. Appl. Math.* **58** 1178–92
[90] Sneyd J, Keizer J and Sanderson M J 1995 Mechanisms of calcium oscillations and waves: a quantitative analysis *FASEB J.* **9** 1463–72
[91] Sneyd J, Tsaneva-Atanasova K, Bruce J I E, Straub S, Giovannucci D V and Yule D I 2003 A model of calcium waves in pancreatic and parotid acinar cells *Biophys. J.* at press
[92] Sun X-P, Callamaras N, Marchant J S and Parker I 1998 A continuum of $InsP_3$-mediated elementary Ca^{2+} signalling events in Xenopus oocytes *J. Physiol.* **509** 67–80
[93] Szado T, Kuo K H, Bernard-Herlay K, Poburko D, Lee C H, Seow C, Ruegg U T and van Breemen C 2003 Agonist induced mitochondrial transients in smooth muscle *FASEB J.* **17** 28–37
[94] Tang Y and Othmer H G 1996 Simplification and analysis of models of calcium dynamics based on IP_3-sensitive calcium channel kinetics *Biophys. J.* **70** 246–63
[95] Taylor C W 1998 Inositol trisphosphate receptors: Ca^{2+}-modulated intracellular Ca^{2+} channels *Biochim. Biophys. Acta* **1436** 19–33
[96] Thomas D, Lipp P, Berridge M J and Bootman M D 1998 Hormone-evoked elementary Ca^{2+} signals are not stereotypical, but reflect activation of different size channel clusters and variable recruitment of channels within a cluster *J. Biol. Chem.* **273** 27130–6
[97] Thomas D, Lipp P, Tovey S C, Berridge M J, Li W, Tsien R Y and Bootman M D 1999 Microscopic properties of elementary Ca^{2+} release sites in non-excitable cells *Curr. Biol.* **10** 8–15
[98] Tinel H, Cancela J M, Mogami H, Gerasimenko J V, Gerasimenko O V, Tepikin A V and Petersen O H 1999 Active mitochondria surrounding the pancreatic acinar granule region prevent spreading of inositol trisphosphate-evoked local cytosolic Ca^{2+} signals *EMBO J.* **18** 4999–5008
[99] Wagner J and Keizer J 1994 Effects of rapid buffers on Ca^{2+} oscillations and Ca^{2+} diffusion *Biophys. J.* **67** 447–56
[100] Wagner J, Li Y-X, Pearson J and Keizer J 1998 Simulation of the fertilization Ca^{2+} wave in Xenopus laevis eggs *Biophys. J.* **75** 2088–97
[101] Wussling M H P and Salz H 1996 Nonlinear propagation of spherical calcium waves in rat cardiac myocytes *Biophys. J.* **70** 1144–53
[102] Yao Y and Parker I 1995 Quantal puffs of intracellular Ca^{2+} evoked by inositol trisphosphate in Xenopus oocytes *J. Physiol.* **482** 533–53
[103] Zimmermann B 2000 Control of $InsP_3$-induced Ca^{2+} oscillations inpermeabilized blowfly salivary gland cells: contribution of mitochondria *J. Physiol.* **525** 707–19